PHYSICAL REVIEW MATERIALS **1**, 043606 (2017)

Shock-wave propagation and reflection in semicrystalline polyethylene: A molecular-level investigation

Robert M. Elder,[1,2,*] Thomas C. O'Connor,[3] Tanya L. Chantawansri,[1] Yelena R. Sliozberg,[1,4] Timothy W. Sirk,[1]
In-Chul Yeh,[1] Mark O. Robbins,[3] and Jan W. Andzelm[1,†]
[1]*U.S. Army Research Laboratory, Aberdeen Proving Ground, Maryland 21005, USA*
[2]*Bennett Aerospace, Inc., Cary, North Carolina 27511, USA*
[3]*Department of Physics and Astronomy, Johns Hopkins University, Baltimore, Maryland 21218, USA*
[4]*SURVICE Engineering Company, Belcamp, Maryland 21017, USA*

(Received 17 May 2017; published 28 September 2017)

Semicrystalline polyethylene (PE) is attractive for a variety of mechanically demanding applications, where shock compression can occur. Although often highly crystalline, PE invariably contains nanoscale amorphous domains that influence shock propagation. Our objective in this work is to study the effects of such domains. To this end, we adopt a novel approach wherein we parametrize a simple continuum-level theory based on the shock impedance from molecular dynamics (MD) simulations. Using this theory, we predict how crystalline/amorphous interfaces attenuate shocks via energy reflection due to the impedance mismatch between the phases. The theory predicts that these interfaces attenuate weak shocks more effectively than strong shocks. We compare the theory to explicit nonequilibrium MD simulations of compressive shocks in semicrystalline PE containing nanometer-scale amorphous regions of varying size, where we analyze the pressure response and reflection of energy. The theory and simulations show good agreement for strong shocks ($\geqslant 1.0$ km/s), but for weak shocks (<1.0 km/s) the simulations show enhanced energy reflection relative to the continuum predictions. Furthermore, the simulations show an effect not captured by the continuum theory: the size of amorphous regions is important. The theory assumes a sharp (discontinuous) interface between two bulk phases and a sharp change in thermodynamic and hydrodynamic quantities at the shock front. However, the simulations show that when amorphous domains are narrow—with widths comparable to the shock front—reflection is reduced compared to the predictions. We identify several nanoscale mechanisms that reduce the impedance mismatch, and thus reduce reflection, at thin amorphous domains. First, the two-wave elastic-plastic structure of shocks in crystalline PE allows the faster-moving elastic precursor wave to compress small amorphous domains before the plastic wave arrives. Second, confinement between stiff, ordered crystalline domains increases the stiffness and chain ordering in small amorphous regions. Moreover, in terms of stiffness the interfaces are similar in width to the shock front, which may contribute to the underprediction of the theory for weak shocks, where the shock front is widest. We conclude by discussing the significance of these results, namely, how they can be applied to tune shock attenuation for particular applications.

DOI: 10.1103/PhysRevMaterials.1.043606

I. INTRODUCTION

Semicrystalline polymers like polyethylene (PE), polypropylene, and nylon are among the most widely used materials for commercial applications. Their compositelike semicrystalline structure produces flexibility and toughness unrealized in typically brittle polymers such as polystyrene or polylactic acid [1]. Various processing techniques, such as gel spinning, can further enhance the strength of these materials by modifying the size, orientation, and proportion of crystallites in the semicrystalline structure [2,3]. Indeed, modern gel-spun PE fibers routinely have crystallinity exceeding 90% and exhibit strength-to-weight ratios rivaling steels. It is unsurprising, then, that gel-spun fibers and fiber-reinforced composites are used in a rapidly expanding number of mechanically demanding applications including prosthetic joints, body armors, shipping cables, and vehicle chassis.

In such applications, the fibers experience sudden impacts that generate mechanical shock waves that mediate failure. Both axial and transverse shock waves propagate from a point of impact, resulting in a complex combination of extension, deflection, and compression [4]. While PE fibers show exceptional strength in tension, their applications are limited by low compressive strengths, where elastic instabilities lead to failure via microbuckling or kinking [5,6]. Thus there is significant interest in studying the shock propagation behavior of these polymer fibers along the in-fiber direction; however, relatively few studies have been devoted to this type of shock [7]. Understanding the transmission and dissipation of shocks within the heterogeneous internal structure of semicrystalline polymers is essential to improve their performance.

A common way to characterize the shock response of a material is to determine its shock Hugoniot; the set of thermodynamic states that a given initial state can transform to after the shock front passes. Alongside experimental efforts [7–11], computational studies have been conducted to determine the shock Hugoniots of crystalline and amorphous PE. A typical method to calculate the shock Hugoniot is to assume that each point on the Rankine-Hugoniot equation corresponds to a state that is in thermodynamic equilibrium, such that the stress state is hydrostatic. Numerous studies have used

---

[*] robert.elder26.ctr@mail.mil
[†] jan.w.andzelm.civ@mail.mil

this method to calculate the shock Hugoniot using either density functional theory (DFT) [12–14] or classical molecular dynamics (MD) [14,15] for crystalline PE, which is the main constituent of PE fibers. The shock behavior of amorphous PE has been studied to a lesser degree using this hydrostatic method [14]. The shock Hugoniot for crystalline PE was also extracted through the uniaxial Hugoniostat method [12], which is another equilibrium technique that uses the Hugoniot relations as constraints without explicitly simulating the shock event [16,17]. Another method is the multiscale shock technique, a combination of MD with the Euler equations for compressible flow [18], which has been used, for example, to calculate the Hugoniot of semicrystalline PE modeled via a novel pressure-transferable coarse-grained model [19]. However, these are equilibrium methods that model the thermodynamic state behind a shock front, rather than the dynamic shock event itself. Explicitly modeling the shock is necessary to study the local, dynamic effects of heterogeneous semicrystalline polymer morphologies.

Here we take an alternative approach using nonequilibrium MD (NEMD), where an explicit shock wave is produced using a virtual piston or flyer plate. In addition to providing the Hugoniot, explicitly modeling the shock yields information like the spatiotemporal evolution of the temperature, pressure, and energy. This methodology has been used for limited PE systems such as amorphous PE [20,21], foams [22,23], and nanocomposites [24], as well as other materials, such as polybutadiene [25,26], phenolic resin composites [27], polyurea [28], and nitromethane liquid/crystal interfaces [29]. However, few efforts have been made to study the interactions between shock waves and the numerous morphological features found in semicrystalline PE, such as the partially amorphous pockets that are invariably present in highly crystalline PE. Interfaces between materials with differing properties, such as crystalline and amorphous PE, can attenuate shock waves through reflection and dispersion [30,31], which can be leveraged for improving energy dissipation in mechanically demanding applications. Thus, examining the effect of these amorphous regions—the objective of this study—will improve our understanding of shock wave propagation in PE.

This paper is organized as follows. In Sec. II we describe the simulation and analysis methods we used to study semicrystalline PE. In Sec. III we provide a brief theoretical background on shock waves, and we review the simple continuum-level theory we use to predict the pressure changes and energy reflection occurring at a single crystalline/amorphous interface. Although the shock impedance is commonly used to interpret simulation results qualitatively, to the best of our knowledge, we are the first to explicitly combine molecular simulations with a quantitative impedance-based theory. In Sec. IV we use NEMD simulations of shocks in purely crystalline PE, purely amorphous PE, and semicrystalline PE containing a single interface, where we explicitly measure energy reflection from the interface. The theory and simulations agree that such interfaces attenuate weak shocks more effectively than strong shocks. Section V is devoted to semicrystalline PE with two interfaces—lamellar models where an amorphous pocket of varying size is sandwiched between two crystalline domains. Here we find that that energy reflection depends on the width of the amorphous domain. In Sec. VI we discuss several molecular-scale factors that influence energy reflection from thin amorphous pockets, namely density, stiffness, and chain ordering. Finally, in Sec. VII we summarize, discuss limitations and future extensions of the present work, and highlight the significance of our results for practical applications.

II. METHODS

A. Overview of systems and conditions studied

We constructed and simulated models of pure PE phases and semicrystalline PE with varying architectures (Fig. 1). The purely amorphous and purely crystalline PE models provide a necessary comparison with the semicrystalline models. The semicrystalline models were constructed with either one or two interfaces between crystalline and amorphous PE. In the one-interface models, one half is crystalline and the other half is amorphous [Fig. 1(a)]. In the two-interface models, an amorphous domain of varying width is sandwiched between two crystalline domains [Fig. 1(b)], similar to the lamellar models introduced by Rutledge and co-workers [32–40]. Other models of semicrystalline PE are possible, for example with randomly oriented crystalline domains that form naturally during long-duration simulations [19], but the idealized one- and two-interface models used here allow us to clearly identify the effects of the interface. The models in this work are summarized in Table I. Ten independent replica configurations of each semicrystalline model were generated to improve sampling. Only one replica configuration was used for the pure phase systems.

Shock waves were generated in these models by impacting them with a rigid piston moving with constant velocity for a period of time [Fig. 1(c)]. The velocities and impact durations used for each model are listed in Table I. A large number and wide range of velocities were used to generate the shock Hugoniots of the pure phases. Fewer velocities—though still spanning the range from weak to strong shocks—were used with the semicrystalline models. Short impact durations of 20 ps were used to observe the transmission of a fixed quantity of energy (a shock pulse) across interfaces. Longer 100 ps impacts, sufficient for the shock to traverse the entire model, were used to observe the long-time behavior of a supported shockwave.

B. Force field

We used a united-atom (UA) model for PE, where each methyl and methylene group is represented as a single UA. This drastically reduces the computational expense compared to all-atom (AA) force fields. This UA force field was developed to reproduce the equilibrium properties and viscosity of alkane melts [41,42] and has been adapted to study the properties of PE [32,38,39]. We have found that equilibrium [14] and NEMD simulations (this work) with this UA force field reproduce the experimentally validated shock Hugoniot of PE (see Fig. S1 in the Supplemental Material [43]). A shortcoming of the UA model is that it does not allow chemical reactivity. However, simulations using a reactive AA force field optimized for high pressures show no bond scission up to 40 GPa [15]. The shocks generated in this work yield maximum pressures below this value, so we do not expect reactivity to play a significant role.

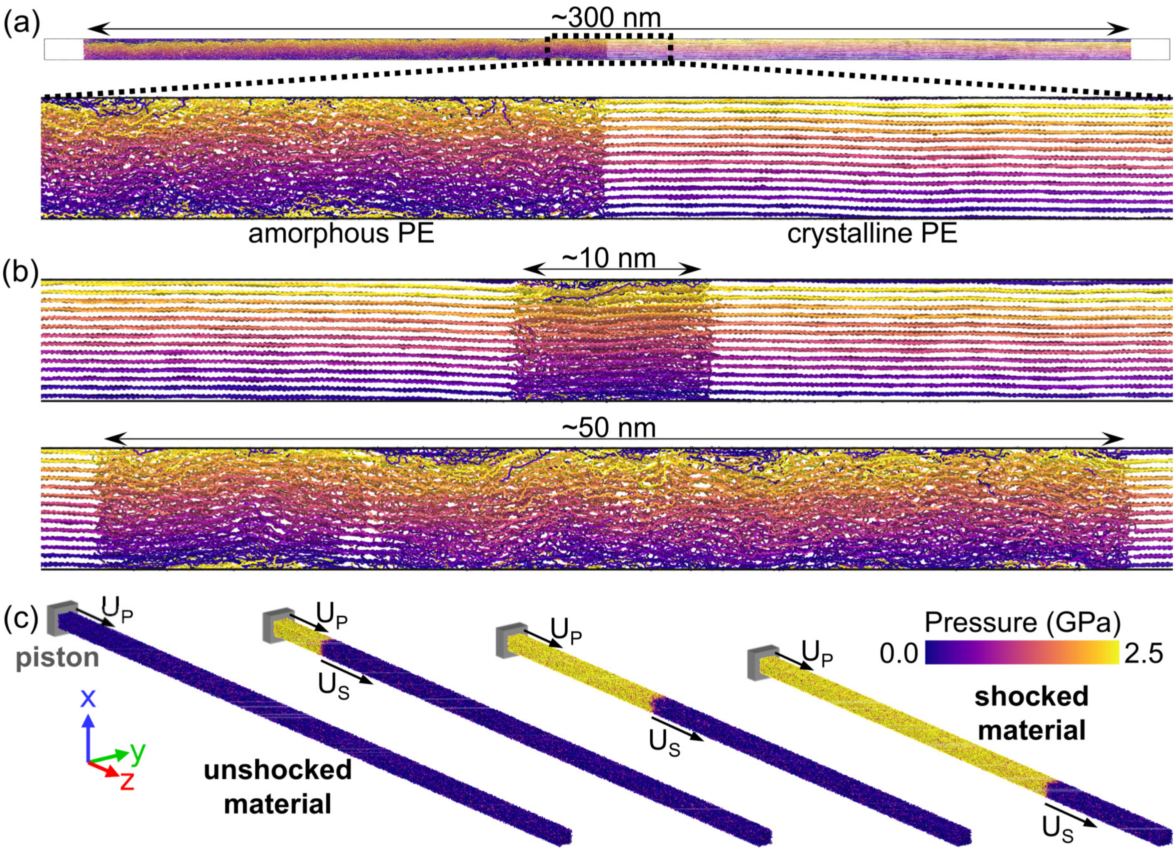

FIG. 1. Models and methods used in this work. (a) One-interface model of semicrystalline PE with one half amorphous and the other half crystalline. Individual polymer chains are colored uniquely. We also constructed purely amorphous and purely crystalline models (not shown). (b) Lamellar models of semicrystalline PE containing an amorphous region of varying length sandwiched between two crystalline domains, yielding two interfaces. (c) Method for producing a shock wave. A planar piston moves with velocity U_P for a period of time, compressing the material, driving up the pressure, and generating a shock wave traveling at velocity $U_S > U_P$.

The functional forms and parameters for the bonded and nonbonded interactions in the UA force field are summarized in Table II. Bonded interactions account for bond stretching, bond angles, and bond torsions. Nonbonded interactions between UAs are described by a Lennard-Jones (LJ) potential. We used a nonbonded interaction cutoff $r_c = 2.5\sigma (10.0225\,\text{Å})$. Nonbonded interactions between UAs separated by fewer than four bonds (i.e., 1–2, 1–3, and 1–4 interactions) are excluded. Inputs for an MD simulation of PE oligomers using this force field are included in the Supplemental Material [43].

TABLE I. Summary of systems and conditions studied in this work.

	Architecture	Piston velocities (km/s)	Impact durations (ps)
Pure phase			
	crystalline (X)	0.1, 0.2, . . . 0.9, 1.0, 2.0, 3.5, 5.0	20, 100
	amorphous (A)	0.1, 0.2, . . . 0.9, 1.0, 2.0, 3.5, 5.0	20, 100
Semicrystalline			
One interface	crystalline/amorphous ($X \rightarrow A$)	0.5, 1.0, 2.0	20, 100
	amorphous/crystalline ($A \rightarrow X$)	0.5, 1.0, 2.0	20, 100
Two interfaces	lamellar stack, crystalline/amorphous/crystalline, width of amorphous domain =		
	5 nm	0.5, 1.0, 2.0	20, 100
	10 nm	0.5, 1.0, 2.0	20, 100
	20 nm	0.5, 1.0, 2.0	20, 100
	50 nm	0.5, 1.0, 2.0	20, 100

TABLE II. Functional form and parameters of UA force field for PE.

Interaction type	Functional form	Parameters
Bond stretching	$E_{b_i} = k_b(l_i - l_0)^2$	$l_0 = 1.53\,\text{Å}$ $k_b = 317\,\text{kcal mol}^{-1}\,\text{Å}^{-2}$
Bond angle	$E_{\theta_i} = k_\theta(\theta_i - \theta_0)^2$	$\theta_0 = 110^\circ$ $k_\theta = 60\,\text{kcal mol}^{-1}\,\text{rad}^{-2}$
Bond torsion	$E_{\phi_i} = \sum_{n=1}^{3} 0.5k_n[1 + (-1)^{n-1}\cos(n\phi_i)]$	$k_1 = 1.6\,\text{kcal mol}^{-1}$ $k_2 = -0.867\,\text{kcal mol}^{-1}$ $k_3 = 3.24\,\text{kcal mol}^{-1}$
Nonbonded (Lennard-Jones)	$E_{\text{LJ}(i,j)} = 4\epsilon_{i,j}\left[\left(\frac{\sigma}{r_{i,j}}\right)^{12} - \left(\frac{\sigma}{r_{i,j}}\right)^{6}\right]$	$\epsilon_{\text{CH}_2-\text{CH}_2} = 0.09344\,\text{kcal mol}^{-1}$ $\epsilon_{\text{CH}_2-\text{CH}_3} = 0.14546\,\text{kcal mol}^{-1}$ $\epsilon_{\text{CH}_3-\text{CH}_3} = 0.22644\,\text{kcal mol}^{-1}$ $\sigma = 4.009\,\text{Å}$

C. Generation of initial coordinates and equilibration protocol

All systems began in a purely crystalline configuration. This initial configuration was generated by replicating the orthorhombic PE unit cell 7 and 11 times in the two lateral (a, b) directions and 1200 times in the axial (c) direction of shock propagation. We aligned the (a, b, c) axes with the (x, y, z) directions of the orthorhombic simulation box, so the chain backbones were aligned in the {001} crystallographic plane. The initial system dimensions were approximately (5, 5, 300) nm along the (x, y, z) Cartesian axes. The system was initially periodic in all three directions, i.e., chains were effectively "infinite" and spanned the periodic boundary in the z direction. We equilibrated this system, as described below, and used it as the basis for all other configurations. The LAMMPS simulation package (http://lammps.sandia.gov) was used for all energy minimization and MD calculations [44].

The initial purely crystalline PE system was first subjected to 10 000 steps each of conjugate gradient and steepest descent minimization. Then, we used MD simulations to equilibrate the temperature (300 K) and pressure (1 atm). A velocity-Verlet integrator with a time step of 2 fs was used. We performed constant volume-constant temperature (NVT) MD with a Langevin thermostat [45] (damping factor = 200 fs) for 100 ps, followed by 100 ps of constant pressure-constant temperature (NPT) MD with the same thermostat and a Berendsen barostat [46] (damping factor = 1000 ps) acting independently on the three periodic dimensions of the simulation cell. Next, we deleted the bonds crossing the periodic boundary and removed the periodicity in the z direction. Thus, all of the PE systems in this work were surrounded by regions of vacuum in the z direction. Using two-dimensional (2D)-periodic systems (i.e., not periodic in the z direction) allowed us to initiate a shock on one side of the system without affecting the other side. Since the models were relatively long in the direction of shock (∼300 nm), we were able to observe the progression of the shockwave for relatively long durations before it reflected from the opposite edge of the system, avoiding the need for reflection-absorbing boundary conditions [47,48]. We repeated the above equilibration protocol (i.e., minimization, temperature equilibration, and pressure equilibration in x and y) with the 2D-periodic system. This equilibrated, 2D-periodic, and purely crystalline model was used as the starting point for constructing semicrystalline and purely amorphous models.

We generated semicrystalline and purely amorphous systems from the equilibrated purely crystalline system using a method involving chain *Deletion*, chain *Cutting*, and *Melting* (*DCM*), which was designed for the present work. For the one-interface systems [Fig. 1(a)], 15% of the chains in the amorphous region were removed in their entirety to reflect the lower density of the amorphous phase. Then 50% of the remaining chains were cut at the interface, and finally 1% of the remaining UAs in the amorphous region were removed to cut the chains into smaller segments. The atoms, bonds, and chains to be removed were chosen randomly. This procedure yielded an amorphous region with roughly the correct amorphous density (chosen as $0.85\,\text{g/cm}^3$), with some chains spanning the interface, and with an average chain length of about 100 united atoms.

The energy of the amorphous region was then minimized with 10 000 steps each of conjugate gradient and steepest descent minimization, equilibrated with NVT MD for 0.8 ns at 600 K to accelerate amorphization (melting), cooled to 300 K over 0.1 ns, and equilibrated at 300 K for 0.1 ns. The coordinates of the crystalline region were fixed until the final 0.1 ns of equilibration. Other details of this equilibration were identical to those used to equilibrate the purely crystalline system (e.g., time step, thermostat). To confine the system in the z direction, walls with a repulsive harmonic potential (spring constant = $10\,\text{kcal/mol/Å}^2$) were placed near the free surfaces. During shock simulations, we used one of the walls as a piston to compress the material [Fig. 1(c)], while the other wall acted as a backstop to prevent any material from exiting the initial simulation box geometry.

To construct the purely amorphous model, we followed a similar *DCM* protocol, removing 15% of the chains and deleting 1% of the remaining atoms in the entire system. For the lamellar semicrystalline models [Fig. 1(b)], we followed the *DCM* protocol but applied it only to a section of given length (5, 10, 20, 50 nm) in the center of the system, and we cut chains at both the crystalline/amorphous and amorphous/crystalline interfaces, randomly selecting 50% of the chains independently at each interface. The chosen dimensions of the amorphous regions (e.g., width of 10 nm) remained constant to within about ±0.5 nm during equilibration. Following these construction procedures, the semicrystalline and purely amorphous systems were used without further equilibration. To improve sampling, ten independent configurations of each semicrystalline model were generated, using randomly initialized velocities and deletions during the *DCM* protocol. All of the models, both pure phase and semicrystalline, contained between ∼310 000 and ∼360 000 atoms depending on the number deleted during the *DCM* protocol.

The *DCM* protocol was sufficient to produce disordered noncrystalline PE that accurately reproduces the shock Hugoniot of amorphous PE (Fig. S1). We adopted this procedure for reasons of computational efficiency in generating numerous models with large amorphous regions. However, the chain statistics (e.g., characteristic ratio, entanglements) differ from those of truly amorphous PE. Likewise, it does not produce accurate chain topologies or interphase structure, the correct construction and properties of which have been the subject of significant interest [32–40,49]. For example, the amorphous chains are partially aligned along the z direction [Figs. 1(a) and 1(b)]. Such alignment can be present in high-performance PE, suggesting that the *DCM* protocol may be more appropriate for studying PE in ultradrawn fibers of ultrahigh molecular weight PE (UHMWPE), rather than more typical PE materials. For the sake of convenience, we use the term "amorphous" for these slightly aligned but noncrystalline regions. To verify that our results are not overly sensitive to the method of amorphization, we used another method to construct a truly amorphous PE model with accurate chain statistics. The truly amorphous model yields the same shock Hugoniot as with the *DCM* model (Fig. S1). Furthermore, this result suggests that our results for energy reflection are likewise insensitive to the method of amorphization, because the shock Hugoniot (or equivalently the shock impedance, as we discuss below) largely dictates energy reflection.

D. Shock simulation protocol and analysis methods

We generated shockwaves by moving a repulsive harmonic wall (the piston) toward the PE system in the z direction at a velocity U_P for a set duration [Fig. 1(c)]. This setup mimics impact with an infinite-impedance flyer plate moving with velocity U_P. We used a velocity-Verlet integrator with a 0.2 fs time step to simulate the dynamics in the microcanonical (NVE) ensemble—corresponding to adiabatic or isentropic shock conditions. After the set duration, the piston stopped and remained stationary at its final position. With a short duration (20 ps), the piston injects a well-defined amount of mechanical energy into the system (a shock pulse), which allowed us to track the partitioning of energy throughout the system over time. Using a longer duration (100 ps), sufficient for the shock to cross the entire model, allowed us to observe the long-time behavior of a supported shock. As our interest is in shock propagation within PE, we primarily focus on the time period *before* the shock has traversed the entire model and reflected from the interface at the far end.

During the simulations, we recorded the profiles (value vs position z) of various properties (e.g., density, velocity) as a function of time. We divided the z direction into 1000 bins (∼3 Å per bin), and averaged values in each bin over 1000 time step (0.2 ps) intervals. The bins were fixed in space. The shock front is associated with a discontinuity in thermodynamic and hydrodynamic variables. To calculate the shock velocity, we tracked the position of the shock front over time by locating the discontinuity in particle velocity. To aid in locating the discontinuity, the velocity profile was smoothed with a 25 bin rolling average to decrease noise; for other analyses, the profiles (e.g., pressure, energy) were analyzed without smoothing to maintain high spatial resolution. We quantified the mean of and uncertainty in the shock velocity as the average and standard deviation from five independent time blocks from each trajectory. The uncertainty was propagated for quantities derived from the velocity [50].

For several analyses we defined regions bounded by two interfaces (i.e., vacuum/crystalline and crystalline/amorphous interfaces) to analyze the properties of those regions, such as the change in total energy. The boundaries of the regions were updated dynamically as the interfaces moved. To identify the vacuum/crystalline interfaces (one on each side of the systems) at a given time, we located the first and last bins containing a nonzero number of atoms. To locate the crystalline/amorphous interfaces initially, we identified discontinuities in the density. We tracked the location of the crystalline/amorphous interfaces over time by assuming they moved with the local particle velocity. This method implicitly assumes that atoms remain in the same phase, i.e., no melting or crystallization occurs at the interface. Direct examination of the structures showed that this assumption was accurate and the interfaces were tracked accurately. The hydrostatic pressure was localized by using the per-atom virial stress [51].

We calculated the width of the shock front (i.e., the distance over which properties transition from quiescent to shocked) by first fitting the particle velocity profile $v(z)$ with a sigmoid function,

$$v(z) = \frac{(v_{\max} - v_{\min})}{1 + \exp\left[\frac{-(z-z_0)}{w}\right]} + v_{\min}, \tag{1}$$

where v is the particle velocity in the z direction, $v_{\min}$ and $v_{\max}$ are the minimum and maximum velocities, z_0 is the center of the shock front and the midpoint of the sigmoid, and w is a fitting constant related to the width. We calculated the width of the shock front as the ratio of the shock height $(v_{\max} - v_{\min})$ to the slope of the sigmoid at z_0. From Eq. (1) this is simply $4w$.

The degree of chain ordering was quantified by first calculating the chain backbone orientation of each united atom i as the vector connecting atoms $i-1$ and $i+1$. This eliminates the alternating orientation of adjacent carbon bonds in the *trans* configuration of crystalline chains. The first and last atoms in each chain were assigned the same orientation as the second and penultimate atoms, respectively. Next, to evaluate the local orientation of chains neighboring atom i, we calculated the average backbone orientation of atoms within 6 Å of atom i, which encompasses the first neighbors of atom i. Then we calculated the angle θ between the local average orientation and the backbone orientation of atom i. This angle was used to calculate the orientational order parameter $P_2 = (3\cos^2\theta - 1)/2$ for each atom [52]. P_2 varies from unity to -0.5, where the upper and lower limits correspond to a backbone orientation parallel and perpendicular to the local average orientation, respectively. When P_2 is averaged over a region containing several atoms, a value of zero indicates the chain ordering is random, as in amorphous PE. We also quantified the alignment of chain backbones with the direction of shock (the $+z$ direction) by calculating the bond orientational order parameter $S_Z = (3\cos^2\theta_Z - 1)/2$, where θ_Z is the angle between the backbone and the z axis [33]. The value of S_Z varies from unity in crystalline PE, where the backbones are oriented in the z direction, to near zero in amorphous PE, where the chains are randomly oriented. Visual Molecular Dynamics (VMD, ks.uiuc.edu/Research/vmd) and the Open Visualization Tool (OVITO, ovito.org) were used for visualization and to facilitate some analysis methods [53,54].

III. THEORETICAL BACKGROUND

The propagation of shock waves across interfaces can be treated with a continuum mechanics approach. Interfaces affect shock propagation due to the sudden change in resistance to shock compression, as measured by the shock impedance Z. The shock impedance of material i can be calculated as $Z_i = \rho_{0,i} U_{S,i}$, where $\rho_{0,i}$ is the preshock density and $U_{S,i}$ is the shock velocity [55,56]. While the shock impedance is a material property, it depends on the shock strength (i.e., piston velocity). The shock Hugoniot from our NEMD simulations and the corresponding shock impedance of crystalline and amorphous PE as a function of shock strength are shown in Fig. 2(a). As the piston velocity increases, the shock impedance increases in both phases, but crystalline PE maintains a higher impedance across the entire range. These results compare favorably with previous theoretical calculations [57], simulations [14,19], and experiments [8], after accounting for variations in crystallinity. For example, the Hugoniot for semicrystalline PE calculated by Oswald and co-workers [19] (∼60% crystallinity) falls midway between the purely crystalline and purely amorphous Hugoniots calculated here.

When a shock wave encounters an interface between materials with different shock impedances, the sudden change in material response generates reflected and transmitted shock waves with different properties than the incident wave. This phenomenon is analogous to the partial reflection/refraction of light waves crossing an interface between media with differing refractive indices. For shock waves, in place of the refractive index, the shock impedance is used to calculate properties of the reflected and transmitted waves. One important property of these new waves is their pressure because, for instance, reflected waves can lead to tensile stresses and material failure through fracture and spalling [58]. A simple analytic equation for the pressure of the transmitted and reflected waves can be calculated assuming nearly linear response [55,59]. The pressure transmission and reflection coefficients are

$$T_P = \frac{P_t}{P_i} = \frac{2Z_2}{Z_2 + Z_1} \tag{2}$$

and

$$R_P = \frac{P_r}{P_i} = T_P - 1 = \frac{Z_2 - Z_1}{Z_2 + Z_1}, \tag{3}$$

where P is the pressure and the subscripts i, r, and t refer to the incident, reflected, and transmitted waves [55].

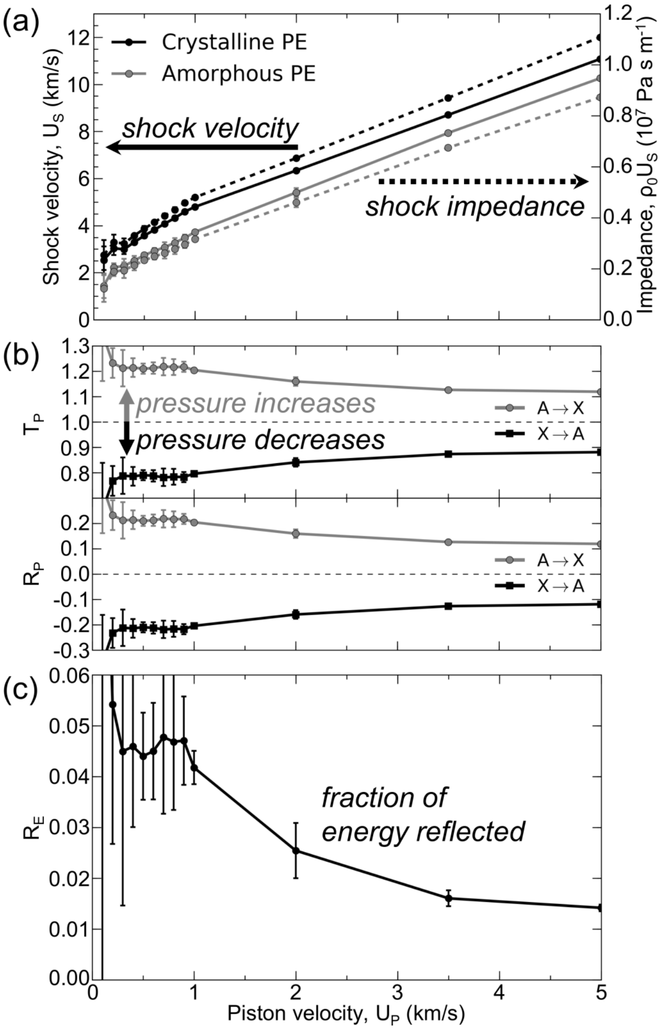

FIG. 2. (a) Shock velocity (solid curves) and shock impedance (dashed curves) of crystalline (X) and amorphous (A) PE. To calculate the shock impedance we used densities ρ_0 of 1.0 and 0.85 g/cm^3 for crystalline and amorphous PE, respectively. Uncertainties are calculated by block-averaging as noted in Sec. II. The uncertainty increases at low piston velocities because the position of the shock front is more difficult to localize. (b) Predicted pressure transmission (T_P, top panel) and reflection (R_P, bottom panel) coefficients for shocks crossing crystalline/amorphous interfaces using the data from (a) in Eqs. (2) and (3). The coefficients depend on whether the wave originates from the amorphous phase ($A \rightarrow X$) or from the crystalline phase ($X \rightarrow A$). (c) Energy reflection coefficient calculated using the shock impedances from (a) in Eq. (4).

The subscripts 1 and 2 refer to the two materials; the incident wave initially propagates through material 1 toward the interface with material 2. In this continuum mechanics approach, the materials are considered homogeneous, we have assumed a planar shock impacting parallel to a planar interface, and the interface and shock wave are approximated as infinitely narrow discontinuities [55]. The pressure of the transmitted/reflected waves depends on the ordering of the two materials [Fig. 2(b)]. For a wave traveling from amorphous to crystalline PE ($A \rightarrow X$) the transmitted pressure is higher than the incident pressure, while with the phases swapped ($X \rightarrow A$) the transmitted pressure is lower. Similarly, relative to the incident pressure, the reflected pressure increases (decreases) when traveling from $A \rightarrow X(X \rightarrow A)$. The transmitted wave is always compressive (positive T_P) because the pressure in the second phase jumps from near zero (ambient conditions) up to the transmitted pressure. Conversely, the reflected wave can be compressive ($A \rightarrow X$, positive R_P) or decompressive ($X \rightarrow A$, negative R_P). Furthermore, the pressure coefficients depend on the shock strength: the magnitude of the pressure change decreases as piston velocity increases, because the impedance mismatch decreases.

The amount of energy reflected and transmitted at an interface can also be predicted using the shock impedance. The fraction of energy reflected is given by the energy reflection coefficient R_E [59,60],

$$R_E = \left(\frac{Z_2 - Z_1}{Z_2 + Z_1} \right)^2. \tag{4}$$

Because Eq. (4) is symmetric with respect to Z_1 and Z_2, energy reflection and transmission are predicted to be independent of the ordering of the materials. As shown in Fig. 2(c), the reflection coefficient is predicted to decrease as the piston velocity increases from 0.5 km/s ($R_E \approx 4.5\%$) to 5.0 km/s ($R_E \approx 1.5\%$). Thus, this continuum mechanics approach predicts that increasing the shock strength will decrease the fraction of energy reflected from crystalline/amorphous interfaces.

The simple analytical theory underlying Eqs. (2)–(4) was developed for elastic waves (linear mechanical response), so it is, at best, qualitative for shock waves (nonlinear, plastic response). Although this theory is successfully applied for elastic waves and even for shock waves in, for example, biomedical applications [60], it is unclear if it is generally accurate for shock waves [59]. Additionally, this theory does not account for the two-wave elastic-plastic structure of shock waves in crystalline PE, for the decompression (or rarefaction) wave that necessarily follows a compressive shock wave [55,61], or for multiple wave reflections, in addition to other factors [62]. Developing rigorous analytical or numerical treatments of shock reflections is nontrivial even in relatively simple geometries (e.g., Refs. [63–65]) and is not the focus of this work. Instead, our intent is to test the qualitative trends predicted by the continuum theory—in particular that energy reflection decreases with increasing piston velocity—and to identify molecular-level mechanisms that influence energy reflection.

IV. SIMULATION RESULTS FOR ONE INTERFACE

We begin by comparing NEMD simulations of shock impinging on a single crystalline/amorphous interface with the above continuum mechanics treatment. We varied the phase from which the shock wave originated (i.e., $A \rightarrow X$ and $X \rightarrow A$). We also conducted shock simulations of purely amorphous (A) and purely crystalline (X) PE phases to compare with the one-interface systems.

A. Pressure response

First we briefly describe the pressure response of purely crystalline and purely amorphous PE during compressive shock loading. We represent the shock simulations with position-time ($z - t$) diagrams, often used to illustrate shock wave propagation and interactions [55,61]. Considering purely amorphous PE, the material is quiescent at $t = 0$ and has a uniform pressure near zero [Fig. 3(a)]. For $t > 0$, the piston displaces the left interface to the right with a fixed speed (1.0 km/s in Fig. 3), compressing the material, driving up the pressure to several gigapascals, and causing a compressive shock wave to propagate through the material to the right with a constant shock velocity. For these simulations, the piston continues moving for the entire duration (100 ps), although we only show results up to 80 ps. At $t \approx 75$ ps, the shock wave reaches the right interface and reflects from the backstop—barely visible as a small light-colored triangle at the upper right of Fig. 3(a). These are the expected behaviors for a shock in an isotropic material like amorphous PE [24].

The shock response of crystalline PE is more complex because its highly anisotropic elastic response leads to a two-wave elastic-plastic structure [Fig. 3(b)]. The elastic precursor wave is acoustic and travels along the chain stems at the longitudinal sound speed (~13 km/s), with little disturbance to chain conformations. This relatively high speed arises from the alignment of the chain backbones, and consequently the large Young's modulus E, in the direction of shock ($E \approx 165$ GPa for this force field at 300 K). The elastic wave speed is given by $(E/\rho)^{0.5}$, yielding a value of ~ 13 km/s. The shock front, a plastic wave, is a true compressive shock with a nearly hydrostatic pressure change. The relevant sound velocity for hydrostatic pressure changes is related to the bulk modulus B, which is much smaller than E. Thus the elastic wave travels more rapidly than the shock in this direction.

The plastic shock wave carries the majority of the impact energy—activating plasticity and significant conformational changes. In this work we primarily focus on the plastic wave, referred to as the shock wave or shock front. The shock velocity in crystalline PE is higher than in amorphous PE [see Hugoniots in Fig. 2(a)], so the shock front reaches the right interface at an earlier time (~60 ps) than in amorphous PE. The pressure is higher in the reflected wave because the backstop effectively has infinite shock impedance, so the pressure reflection coefficient approaches $R_P = 1$ [Eq. (3)].

The shock pressure may be expressed in terms of the impedance as $P = ZU_P$ [55]. Since the impedance is always greater in the crystalline phase, we expect crystalline shock pressures to always exceed amorphous pressures at fixed U_P. This is shown for shocks in crystalline and amorphous PE with $U_P = 1.0$ km/s in Figs. 3(a) and 3(b). We observe consistent trends across the range of piston velocities studied.

In the one-interface systems, the pressure response shows several interesting features. In the $A \rightarrow X$ system [Fig. 3(c)], the pressure response in the amorphous region is identical to the purely amorphous system until the shock wave reaches the amorphous/crystalline interface. Upon reaching the interface at ~40 ps, reflected and transmitted shock waves are generated. Since crystalline PE has a higher shock impedance than amorphous PE, the reflected and transmitted pressures increase relative to the incident wave, in agreement with the calculated pressure transmission/reflection coefficients [Fig. 2(b)]. Thus, the reflected wave is compressive and has a sharp, well-defined front [55,56,61]. The transmitted wave in the crystalline region is qualitatively similar to the shock in the purely crystalline system (e.g., two-wave structure). The reflected wave itself

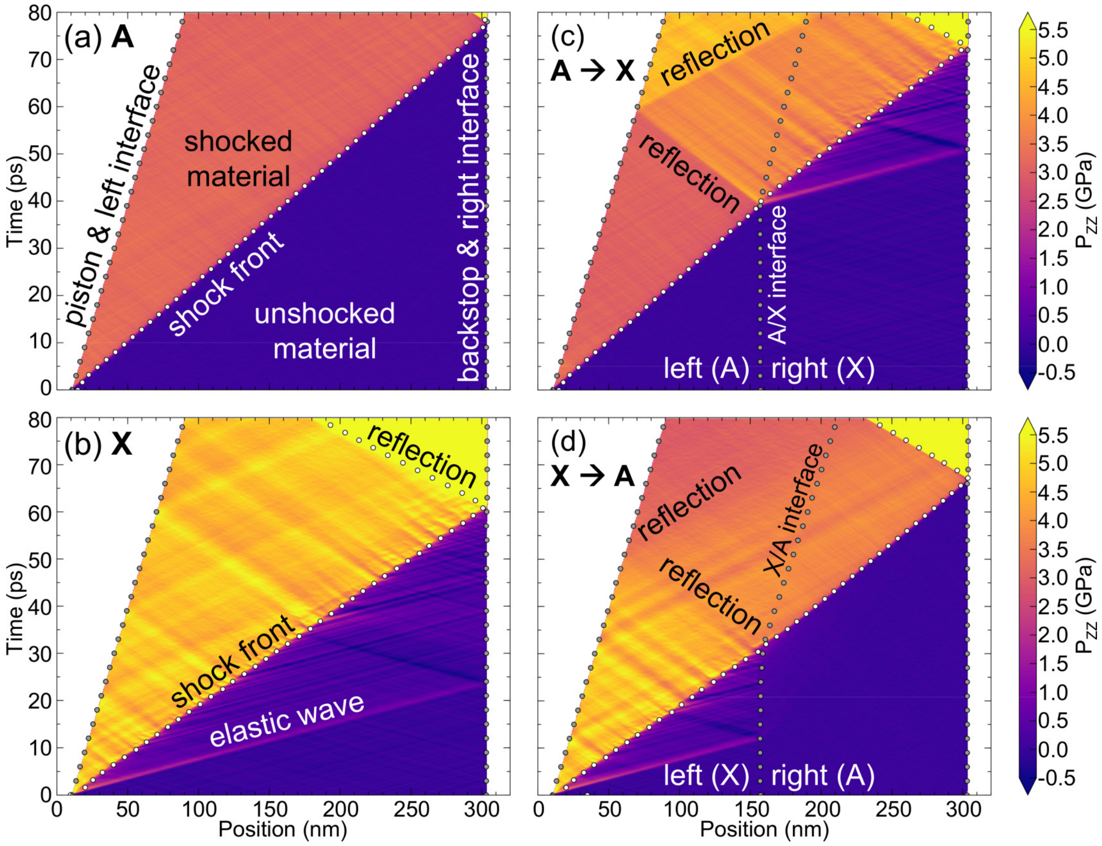

FIG. 3. Position-time ($z - t$) diagrams of pressure parallel to the shock P_{ZZ} for a shock with piston velocity = 1.0 km/s in (a) amorphous PE (A), (b) crystalline PE (X), (c) one-interface system $A \rightarrow X$, and (d) one-interface system $X \rightarrow A$. Interfaces (crystalline/amorphous or PE/vacuum) are indicated by light gray circles, and the shock front is labeled with white circles. White areas correspond to regions of vacuum. These results are for one representative replica configuration.

reflects from the piston at ~60 ps, increasing the pressure because the piston effectively has infinite shock impedance.

In the $X \rightarrow A$ system [Fig. 3(d)], the reflected/transmitted pressures are lower than the incident pressure, and the reflected wave is a decompression wave rather than a compressive wave, in agreement with the pressure coefficients from Eqs. (2) and (3) [Fig. 2(b)]. The reflected decompression wave is not steady and broadens over time, decomposing into acoustic waves [55,56,61]. Upon reaching the piston at ~50 ps, the reflected wave itself reflects to produce an even lower pressure, as expected for a decompression wave incident on a material with higher (infinite) impedance [55,61].

The pressure changes in NEMD simulations can be compared directly with the continuum theory by examining the spatial profiles of the pressure before and after reflection [Fig. 4(a)]. For example, in the $A \rightarrow X$ system at $U_P = 1.0$ km/s, the incident pressure of ~3.1 GPa jumps to ~3.9 GPa in the transmitted wave [Fig. 4(a)], indicating a pressure transmission coefficient of $3.9/3.1 \approx 1.26$. Similar calculations for both single-interface systems at each piston speed are summarized in Fig. 4(b). In the $A \rightarrow X$ system we observe the correct qualitative trend with increasing piston velocity, that is, T_P decreases. Quantitatively, the agreement is generally good, although at lower piston velocities the simulations show larger transmission coefficients than predicted by the theory. In the $X \rightarrow A$ system we find quantitative agreement across the range of shock strengths. Overall these results demonstrate good agreement between the continuum-level calculations and molecular simulations, although the agreement declines somewhat for weaker shocks in the $A \rightarrow X$ system for reasons we discuss in Sec. VI.

B. Energy reflection

Understanding energy propagation and dissipation in heterogeneous semicrystalline materials is particularly important for improving their toughness and durability in mechanically demanding applications. As a means of quantifying the reflection of energy from a crystalline/amorphous interface, we monitor the total amount of energy on either side of the interface, the left and right regions, in each system. As shown in Fig. 3, the boundaries of the two regions were updated dynamically as the interfaces moved. We deposit a fixed quantity of energy by generating a finite shock pulse (20 ps of piston motion). Then we track the change in energy in the two regions, observing how much energy the pulse transmits across the interface. Comparing the one-interface systems with the appropriate pure system, corresponding to the phase of initial impact, then allows us to determine the fraction of energy that is reflected from the interface. The position of the dividing line between the left and right regions in the pure systems, which of course do not contain an interface, is chosen such that the

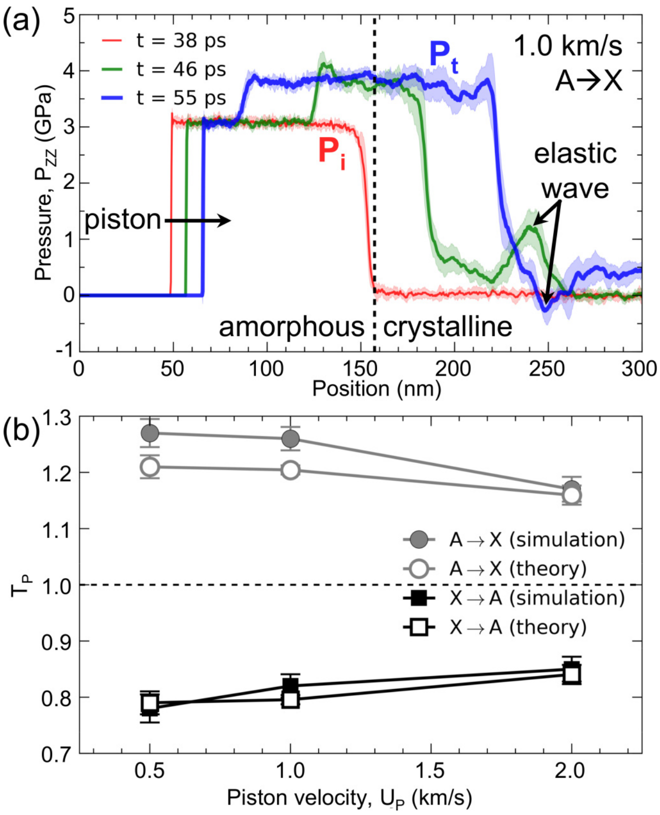

FIG. 4. Pressure reflection/transmission during shock simulations. (a) Pressure parallel to the direction of shock P_{ZZ} at three different times in the $A \rightarrow X$ system during a 1.0 km/s impact. The elastic wave in the crystalline phase ($t = 46$ ps), and its reflection from the backstop ($t = 55$ ps), are labeled. The vertical dashed line indicates the initial position of the amorphous/crystalline interface. The shaded areas show the standard deviation of ten replica structures. (b) Pressure transmission coefficients T_P from simulations compared to the continuum theory [Eq. (2)]. The pressure reflection coefficients R_P are simply $T_P - 1$ [Eq. (3)].

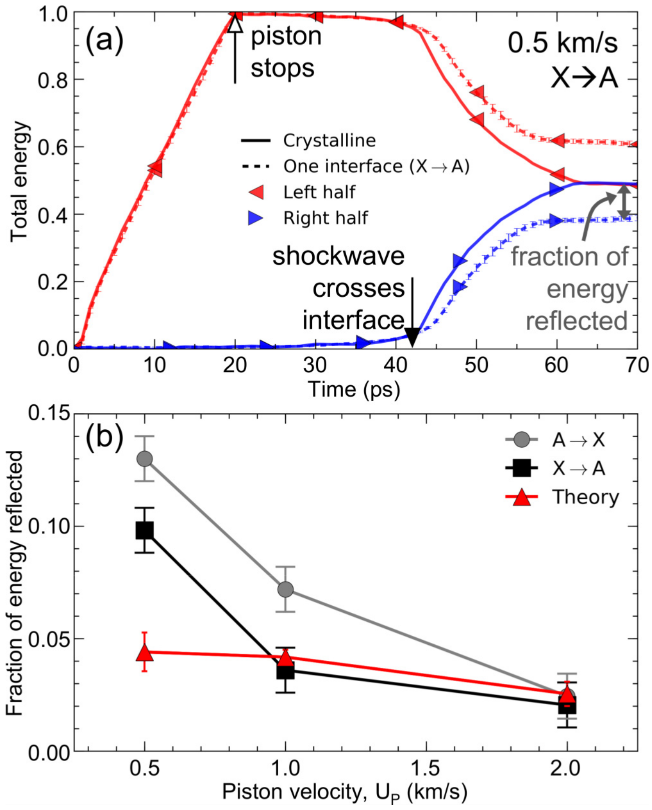

FIG. 5. (a) Change in total energy (kinetic plus potential) in the left and right regions of the $X \rightarrow A$ and purely crystalline systems during and after an impact pulse with a piston moving at 0.5 km/s. Values are normalized by the amount of energy input by the piston. The open arrow shows when the piston stops moving (20 ps). The filled arrow shows when the shock wave crosses the interface. Error bars are the standard error of ten replicas and are smaller than the symbols. (b) Energy reflection in the one-interface systems as a function of piston velocity. We quantify energy reflection as the difference between the energy in the right region of the pure phase and semicrystalline models at long times, as illustrated in (a). Data labeled "Theory" is from the continuum calculations [Fig. 2(c) and Eq. (4)].

length of the left region is equal in the pure and semicrystalline systems; the boundaries of the regions are updated dynamically as noted in the methods.

We first describe this analysis for the purely crystalline and $X \rightarrow A$ systems impacted with a piston moving at 0.5 km/s [Fig. 5(a)], which is exemplary of the other systems and impact conditions. Before the piston begins moving ($t < 0$), the change in total energy is zero in both the left and right regions. As the piston compresses the material (0 to 20 ps), the energy in the left region increases (red curves). The energy saturates when the piston stops at 20 ps, and we normalize the energies in Fig. 5 by this input energy. The energy change in the right region (blue curves) remains near zero until the elastic precursor wave arrives at around 15 ps, but the majority of the energy remains in the left region until the shock wave reaches the interface at about 45 ps. Over the next 15 ps, about 40%–50% of the energy crosses the interface into the right region, while the balance of the energy remains in the left region. To determine the effect of the interface, we compare the fraction of energy that reaches the right region at long times (here, ~70 ps) in the two systems. In the purely crystalline system ~50% of the energy reaches the right region [solid blue curve in Fig. 5(a)], compared to only ~40% in the $X \rightarrow A$ system (dashed blue curve). The difference of ~10% indicates that the crystalline/amorphous interface reflected ~10% of the incident energy.

The same analysis for other shock strengths and system geometries is summarized in Fig. 5(b). The fraction of energy reflected decreases with increasing piston velocity, regardless of the ordering of the two phases, in agreement with the continuum predictions. Furthermore, the reflection coefficients from the MD simulations agree quantitatively with the continuum theory in the limit of strong shocks ($U_P \approx 2.0$ km/s). However, as the shock strength is reduced, the simulations develop an asymmetry depending on the phase from which the shock originated, with the $X \rightarrow A$ system consistently showing lower reflection. This result is contrary to the theory, where energy reflection is independent of the ordering of the phases. Moreover, for weak shocks, the simulated reflection coefficients are consistently larger than the theory predicts. These interesting discrepancies may arise for the reasons discussed in Sec. III (e.g., this simple theory disregards some continuum-level physics) and for reasons discussed in Sec. VI—that is, molecular-level mechanisms that would be difficult to account for *a priori*.

V. TWO INTERFACES

Next we consider a model of an amorphous inclusion in highly crystalline PE; a lamellar model in which an amorphous region of varying size is sandwiched between two crystalline domains, resulting in two crystalline/amorphous interfaces. We have simulated lamellar models where the amorphous inclusion has thicknesses of 5, 10, 20, and 50 nm, which covers the size distribution of such regions in highly aligned PE [3]. We mainly focus on 10 and 50 nm regions—referred to as L10 and L50—as representative of smaller and larger amorphous domains.

A. Pressure response

The pressure response of the lamellar semicrystalline models is qualitatively similar at all velocities studied, so for brevity we only present data for a piston velocity of 1.0 km/s (Fig. 6). In the L50 system [Fig. 6(a)], the initial response in the left crystalline region resembles that of the purely crystalline system [Fig. 3(b)], with an elastic precursor wave and a slower-moving plastic wave. The precursor wave arrives at the first interface at around 10 ps, where it is partially absorbed by the amorphous domain. When the shock front reaches the first interface at about 25 ps, we observe a reflection and reduction in pressure comparable to the behavior in the single-interface $X \rightarrow A$ system [Fig. 3(d)]. The shock front travels smoothly through the amorphous region in a manner resembling purely amorphous PE [Fig. 3(a)]. As the shock front reaches the second interface at about 35 ps, we observe a reflection, an increase in pressure, and the emission of an elastic precursor wave similar to that in the $A \rightarrow X$ system [Fig. 3(c)]. Finally, the shock continues through the right crystalline domain until reaching the edge of the system at about 60 ps. All of these behaviors are consistent with our expectations from the continuum theory and from MD simulations of one-interface systems.

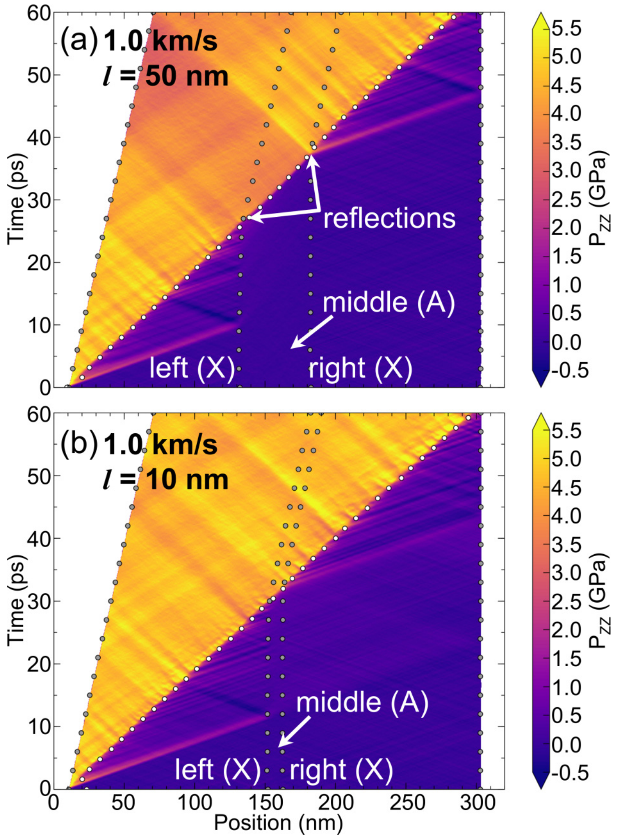

FIG. 6. Position-time ($z - t$) diagrams of pressure for shock with piston velocity = 1.0 km/s in lamellar semicrystalline models with amorphous domains of widths (a) $l = 50$ nm (L50) and (b) $l = 10$ nm (L10). The piston is in motion for the entire duration of the simulation. The left, middle, and right regions are labeled as crystalline (X) or amorphous (A). Results are for a representative replica.

The pressure response of the L10 system is markedly different [Fig. 6(b)]. The signatures of reflection—pressure changes—are absent in the L10 system, despite having the same two-interface architecture as the L50 system. This deviation from the continuum-level calculations suggests that nanoscale effects become significant as the thickness of the amorphous layer is reduced. In the following sections, we further examine the absence of reflection and explanations for this phenomenon.

B. Energy reflection

Bearing in mind the differing pressure responses of the L10 and L50 systems, we perform shock pulse simulations to study energy transmission through the amorphous domains. We divide the lamellar semicrystalline systems into three regions: left (crystalline), middle (amorphous), and right (crystalline). Similarly, we divide the purely crystalline system into three regions, with boundaries based on the semicrystalline systems, such that the length of the left and middle regions was equal in the pure and semicrystalline systems. By monitoring the change in energy in these regions over time, we determine how much energy is blocked by the amorphous layer. The general features of these energy diagrams [Fig. 7(a)] are analogous to the one-interface systems [see above description of Fig. 5(a)]. We compare the effects of piston velocity and width of the amorphous region on reflected energy in Fig. 7(b).

For an amorphous region with a given width, increasing the piston velocity decreases reflection, in agreement with the theoretical calculations and one-interface MD simulations. More interestingly, the simulations show an effect not captured by the theory: thinner amorphous regions reflect less energy. Additionally, the amount of energy reflected from two interfaces is less than would be expected based on the one-interface simulation results. For example, for $U_P = 0.5$ km/s the energy reflection from a single interface is roughly 10% [Fig. 5(b)], suggesting that two consecutive interfaces should yield roughly 20% reflection. However, we observe only ∼10% reflection from the 50 nm region, and even less from narrower regions [Fig. 7(b)].

To validate the trend of reduced reflection from narrower amorphous regions, we employed additional techniques to

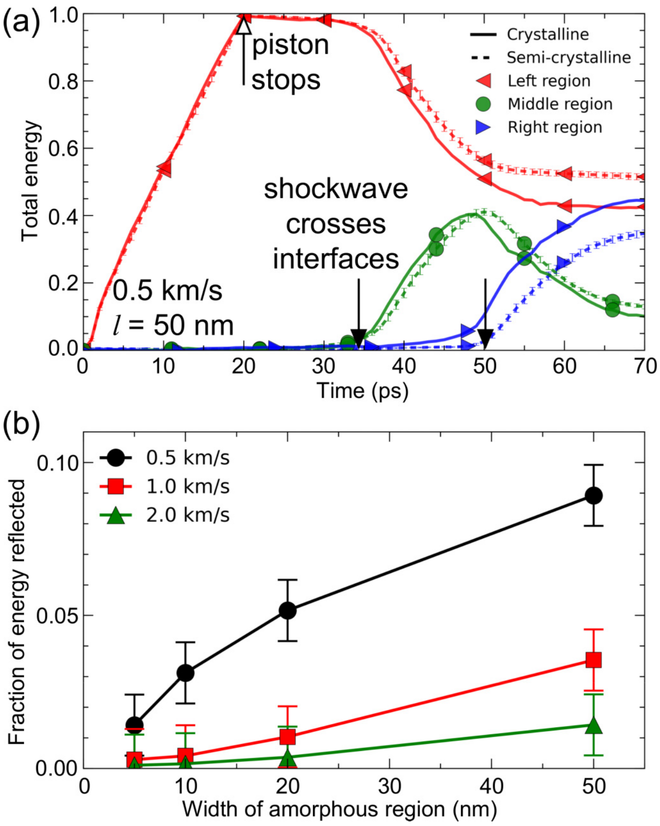

FIG. 7. (a) Change in total energy (kinetic plus potential) in the left, middle, and right sections of purely crystalline (solid curves) and lamellar semicrystalline (dashed curves) models during and after an impact with piston velocity $U_P = 0.5\,\mathrm{km/s}$. Values are normalized by the total amount of energy imparted by the piston. The open arrow shows when the piston stops moving (20 ps). The filled arrows show when the shock wave crosses the two interfaces. Error bars are as in Fig. 5(a). (b) Fraction of energy reflected in the lamellar semicrystalline models as a function of piston velocity and width of the amorphous region.

quantify energy reflection. The energy flux imparted by the piston can be expressed as the product of the shock pressure and the particle velocity PU_P [66]. Additionally, we calculated the local energy flux using another method involving the local energy and stress decomposed on a per-atom basis, e.g., as in Ref. [67]. Upon crossing an interface, the pressure, particle velocity, local energy, and local stress change due to the differing impedances, which reduces the energy flux due to the impedance mismatch. The fractional decrease in energy flux across the amorphous domain is another measure of energy reflection. Although the quantitative results vary between methods, the qualitative trends in the energy-pulse results [Fig. 7(b)] also appear in the energy-flux results (Figs. S2 and S3). We also attempted to use the energy flux to quantify reflection in the one-interface systems, but we found inconsistent results that we have been unable to fully reconcile, as discussed in the Supplemental Material (Fig. S4) [43]. Nonetheless, the consistency of the two-interface results across multiple analysis methods provides support for the key trend—that is, thinner amorphous domains reflect less energy.

VI. FACTORS INFLUENCING ENERGY REFLECTION

We examine several aspects of the amorphous domains: density; and confinement-induced stiffening and chain ordering/alignment. Taken together, these factors provide useful insights and a plausible explanation for the reduced reflection from narrow amorphous regions.

A. Density

The most significant factor appears to be the density of the amorphous region, which directly affects the impedance (i.e., $Z = \rho U_S$). Although each amorphous region was constructed with the same initial density ($0.85\,\mathrm{g/cm^3}$), the density changes over time during the shock simulations (Fig. 8). Before the arrival of the plastic shock front, the impact of the faster-moving elastic precursor wave compresses the amorphous regions. (The precursor wave is easier to identify using the pressure, Fig. 6). As a result, the density of the 10 nm region rapidly increases from 0.85 to $0.97\,\mathrm{g/cm^3}$, just below the density of crystalline PE, $1.00\,\mathrm{g/cm^3}$ [Fig. 8(c)]. Increasing the density increases the shock impedance of the amorphous region, thereby decreasing the impedance mismatch and energy reflection. To illustrate this idea, we determined the Hugoniot of amorphous PE that was pre-compressed to a density of $0.97\,\mathrm{g/cm^3}$ [68]. The Hugoniot for the compressed amorphous PE is shifted upward toward that for crystalline PE [Fig. 8(d)]. Consequently, the impedance mismatch is nearly eliminated, which suggests this mechanism is the dominant factor in reducing energy reflection from narrower amorphous regions. In contrast, the average density of the larger L50 amorphous regions reaches only $0.88\,\mathrm{g/cm^3}$ before impact by the plastic wave. As a result, energy reflection is reduced by a lesser extent in larger amorphous regions.

Furthermore, precompression by the elastic wave provides an explanation for the asymmetry of reflection observed in the single-interface systems, where reflection is systematically lower in the $X \rightarrow A$ system than the $A \rightarrow X$ system [Fig. 5(b)]. The elastic precursor wave in the crystalline region of the $X \rightarrow A$ system compresses the amorphous material near the interface before the shock arrives, reducing both the impedance mismatch and energy reflection. Additionally, precompression creates a density and therefore impedance gradient across the interface, which has a nontrivial influence on reflection (e.g., Refs. [63,69], and see discussion below). We note that experiments on the axial propagation of shock waves in highly aligned PE demonstrated the existence of elastic precursor waves [7]. It is therefore plausible that this mechanism is active in experimental samples of PE.

B. Confinement effects: Stiffness and chain ordering

The stiffness of soft materials confined in thin films can be elevated substantially over bulk values [70–74]. We observe similar effects in the amorphous regions of our semicrystalline models, confined between two stiff crystalline regions. Both sound speed and shock impedance increase with stiffness [55], reducing the impedance mismatch and, therefore, energy reflection. We quantified this effect by measuring the atomic-scale mobility in our semicrystalline models. We quantify atomic mobility by calculating the

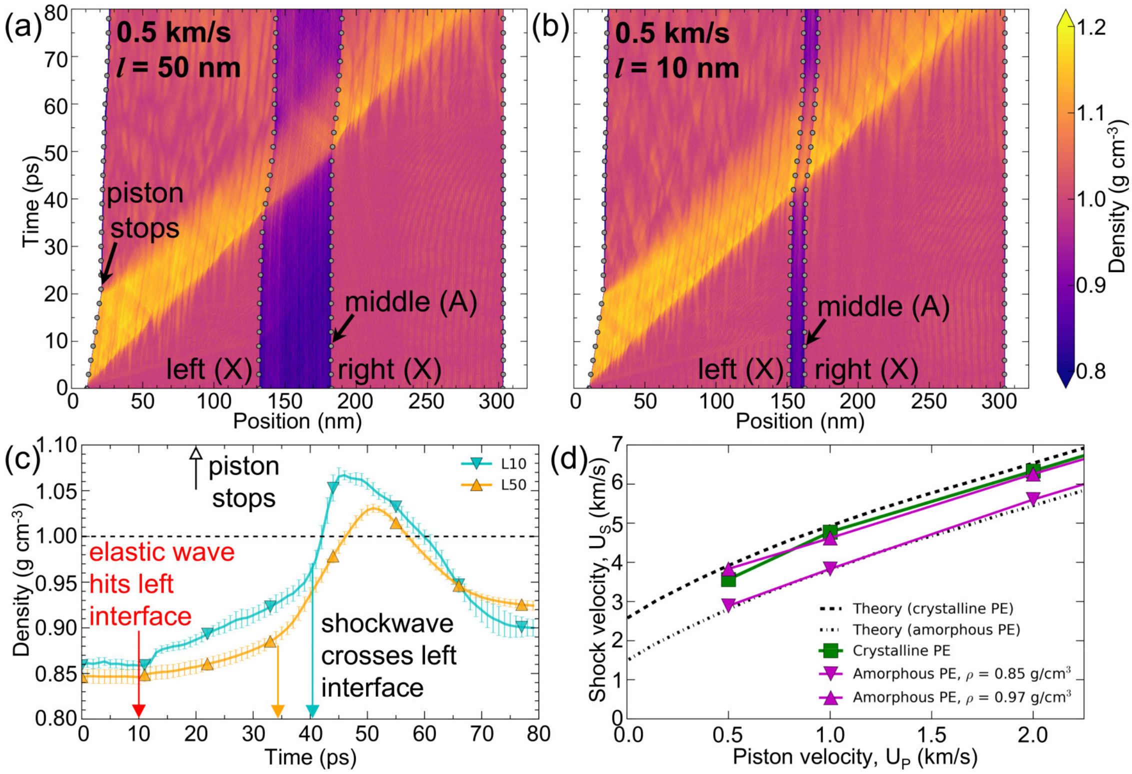

FIG. 8. Density in the lamellar semicrystalline models. (Top row) Position-time diagrams of density for a shock with piston velocity $= 0.5\,\mathrm{km/s}$ in lamellar semicrystalline models with amorphous regions of length (a) $l = 50\,\mathrm{nm}$ (L50) and (b) $l = 10\,\mathrm{nm}$ (L10). The left, middle, and right regions are labeled as crystalline (X) or amorphous (A). (c) Average density in the middle (amorphous) region. The open arrow shows when the piston stops moving (20 ps). The filled arrows show when the shock wave crosses the left interface in each system. The filled red arrow shows when the elastic precursor wave hits the left crystalline/amorphous interface. The dashed horizontal line indicates the density of crystalline PE ($1.0\,\mathrm{g/cm^3}$). (d) Shock Hugoniot of crystalline PE, amorphous PE with typical density ($0.85\,\mathrm{g/cm^3}$), and amorphous PE precompressed to the density reached by the amorphous region in the L10 systems ($0.97\,\mathrm{g/cm^3}$). The curves labeled as "Theory" are data from Ref. [57].

root-mean-square fluctuation (RMSF) of each united atom i over a period of time τ:

$$\mathrm{RMSF}_i = \sqrt{\frac{1}{\tau}\sum_{t=1}^{\tau}\|\boldsymbol{r}_i(t) - \boldsymbol{r}_{i,\,\mathrm{mean}}\|^2}, \tag{5}$$

where $\boldsymbol{r}_i(t)$ is the position in each snapshot t, and $\boldsymbol{r}_{i,\,\mathrm{mean}}$ is the average position during the time period. Larger values of RMSF indicate greater mobility [75,76]. We plot mobility measurements in Figs. 9(a) and 9(b). As expected, the atomic mobility is lower in the crystalline phase than in the amorphous phase, except at the free surfaces where mobility is enhanced [77]. The amorphous mobility declines as the amorphous region is narrowed. From the mobility, we calculate an effective local stiffness k by applying the equipartition theorem and treating the atoms as independent harmonic oscillators (i.e., an Einstein solid) $k = k_B T/\mathrm{RMSF}^2$, where k_B is the Boltzmann constant and T is the temperature [78]. The trends in stiffness are inverted in the mobility, with smaller amorphous regions having higher stiffness [Figs. 9(c) and 9(d)]. From $l = 50\,\mathrm{nm}$ to $l = 5\,\mathrm{nm}$, we observe a local stiffness enhancement of ~20%.

The bulk sound speed C_B is related to material stiffness as $C_B = \sqrt{K/\rho}$, where K is the bulk modulus and ρ is the density. K is expected to scale with the local stiffness k, which could in principal be quantitatively related to the energy reflection coefficient through the shock speed and impedance. If we naïvely assume $Z = \rho U_s \sim C_B \sim k^{1/2}$, then a 20% enhancement of local stiffness would correspond to ~10% increase in Z for the amorphous phase. Applying this in Eq. (4), the prediction for R_E decreases by ~38% at $U_P = 1.0\,\mathrm{km/s}$. Such impedance corrections can describe (within error bars) the trends in R_E for $U_P \geqslant 1.0\,\mathrm{km/s}$ [Fig. 7(b)]. However, they fail to fully explain the dramatic decrease in R_E with decreasing amorphous width for $U_P = 0.5\,\mathrm{km/s}$ (weak shock), so both density *and* stiffness effects must contribute to this trend. They also fail to account for the energy reflection of the amorphous layer being significantly less than we would expect from two independent interfaces ($X \rightarrow A$ and $A \rightarrow X$), which suggests that the precompression effect is still active in even the largest amorphous pockets studied here. Thus, greater energy reflection can be achieved with even larger (>50 nm) amorphous regions.

Examining the interface closely reveals that the transition from crystalline to amorphous stiffness occurs over a distance of ~$10 - 15\,\mathrm{nm}$ [Fig. 9(d)]. This demonstrates that, in terms of stiffness, the crystalline/amorphous interface is rather broad. This is in contrast to other properties, like density, which transition sharply over ~2 nm. Although much of the transition

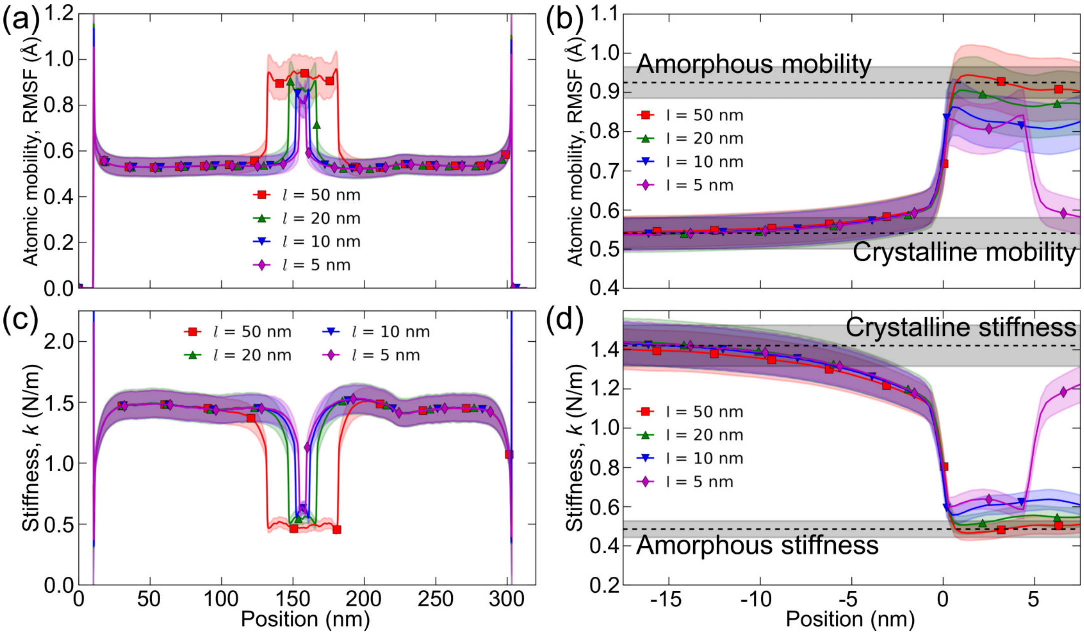

FIG. 9. Nanoscale atomic mobility and stiffness in lamellar semicrystalline PE models. (a) Atomic mobility (root-mean-square fluctuation, RMSF) of the entire model. (b) Detailed view of atomic mobility near the interface, with the curves shifted to align the left interface of all models. Position is relative to the left interface. (c) Stiffness of the entire configuration. (d) Detailed view of stiffness near the interface, with curves shifted as in (b). These data were acquired from equilibrium MD simulations (no shock wave). We show results using $\tau = 20$ ps in Eq. (5). The results are qualitatively similar for other time periods (2 and 200 ps); in particular, the amorphous mobility decreases by roughly the same fraction with decreasing width. The profiles are averaged over 1000 independent samples from 2 ns simulations with each replica structure. The shaded regions show the standard deviation. The horizontal lines show the values for purely amorphous and purely crystalline PE.

between crystalline and amorphous stiffness does occur over a region of ∼2 nm, a broad transition region extends another ∼10 nm into the crystalline domain. Thus, there is a gradient of stiffness and impedance across the interface. Relative to a sharp interface, such a gradient influences reflection in complex ways that depend on the gradient and material properties [63,69]. A notable application of impedance-graded materials is to attenuate shock waves while avoiding the problem of reflected waves inducing fracture in layered composites [79]. Moreover, these observations have implications for continuum mechanics calculations. For convenience, it is typical to treat interfaces and shock waves as discontinuities with vanishingly small width, which is generally a good simplifying assumption [55,61]. This assumption breaks down when features of the system (e.g., grains in polycrystalline materials, amorphous domains in semicrystalline materials) have sizes similar to the shock width. In reality, shock waves have finite width, ranging from $\sim 2-20$ nm in our simulations, depending on the PE phase and the shock strength (Fig. 10). Hence, the interface and shock front have finite and comparable widths. These observations help establish a length scale below which the sharp-interface assumption becomes less reliable.

The breakdown of the sharp-interface assumption has implications for shock wave attenuation in semicrystalline PE. It coincides with the larger-than-predicted pressure changes [Fig. 4(b)] and energy reflection [Fig. 5(b)] for weak shocks, where the shock front is widest and thus deviates most from the assumption. Likewise, it coincides with the asymmetry observed in the one-interface systems, where reflection in the $X \rightarrow A$ system is closer to the theoretical predictions than in the $A \rightarrow X$ system [Fig. 5(b)]. Shocks in crystalline PE, the initial phase in the $X \rightarrow A$ system, are narrower and therefore closer to the theoretical assumption [Fig. 10(b)]. A shock width comparable to the amorphous lamella thickness could also lead to a coupling of the two reflection events, modifying the total energy reflected relative to two independent reflections. At present, we can only postulate a connection between finite shock width and the observed reduction in R_E across amorphous layers. Rigorous treatment will require a different approach in which the width of interfaces/shock fronts can be varied independently of other factors, such as stiffness and density.

Lastly, interfacial amorphous chains exhibit enhanced ordering due to their proximity to the crystalline phase [33,34]. Enhanced ordering of chain backbones increases stiffness by hindering conformational freedom of amorphous chains, and therefore decreases the impedance mismatch. We quantify chain ordering (with respect to neighboring chains) and chain alignment (with respect to the shock direction) with the orientational order parameters P_2 and S_Z, respectively. Values of these parameters near unity indicate good ordering/alignment, as in crystalline PE, while values near zero indicate random ordering/alignment. The average ordering P_2 in the larger L50 amorphous regions is around 0.4 [Fig. 11(a)], whereas the smaller L10 amorphous regions are more ordered, with values around 0.7 [Fig. 11(b)]. Likewise, chain alignment S_Z is elevated in smaller amorphous domains [Figs. 11(c) and 11(d)]. Therefore, ordering and alignment are also associated with reduced reflection from thinner amorphous domains.

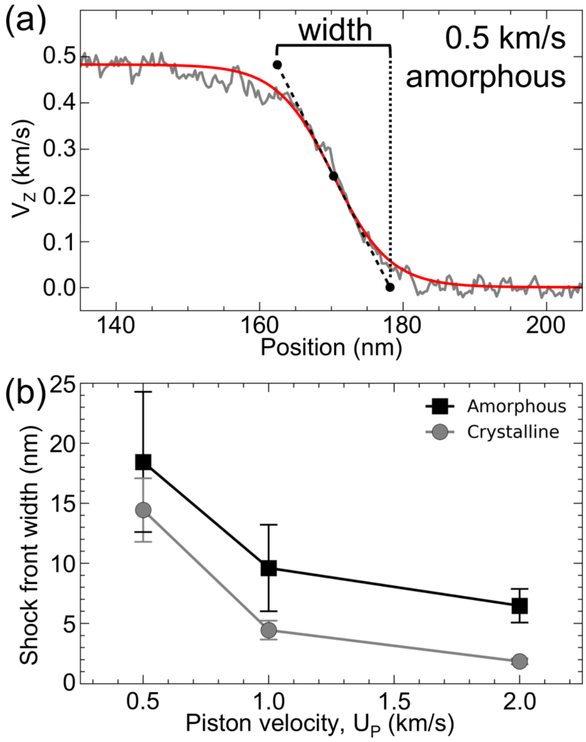

FIG. 10. Width of the shock front. (a) Example of sigmoidal fit to Eq. (1) (red curve) to the velocity profile (gray curve) to find the shock width in amorphous PE with $U_P = 0.5$ km/s. The black points and dashed line demonstrate our definition of width. (b) Shock front width in crystalline and amorphous PE as a function of piston velocity. Error bars are the standard deviation over the entire 100 ps trajectory.

VII. CONCLUSION

We used nonequilibrium molecular dynamics simulations to study well-aligned semicrystalline polyethylene under compressive shock loading conditions. We began by considering shock propagation through a single crystalline/amorphous interface by parametrizing a simple continuum-level theory based on the shock impedance, and by explicitly simulating compressive shocks using NEMD simulations. The impedance mismatch at an interface between two materials attenuates shock waves via the partial reflection of energy. The theory and simulations agree that energy reflection decreases with increasing shock strength, such that weak shocks are attenuated more effectively than strong shocks. However, for weak shocks the simulations demonstrate greatly enhanced energy reflection relative to the theory. Next, we studied lamellar models with two interfaces, in which an amorphous domain of varying size is sandwiched between two crystalline regions. With sufficiently large amorphous regions, we observed significant energy reflection, as expected. However, the simulations show an effect not captured by the theory: when the amorphous domains are thin—with widths comparable to the shock width—reflection is greatly reduced compared to the predictions. Additionally, the reflection from two interfaces is lower than expected based on simulations with a single interface.

We identified two nanoscale mechanisms that reduce the impedance mismatch, and therefore reflection, at thin amorphous regions. First, shocks in crystalline PE have a two-wave elastic-plastic structure, with the elastic precursor wave moving more rapidly than the plastic wave. The early arrival of the precursor wave compresses small amorphous regions, raising their density toward that of crystalline PE and reducing the impedance mismatch. Second, the stiffness of small amorphous domains is significantly higher than bulk amorphous PE due to confinement between stiff crystalline PE regions, with the stiffness decreasing with increasing width. Impedance mismatch is also reduced for narrower regions because they have higher chain ordering and alignment due to their proximity to the well-ordered crystalline phase. Finally, the width of the high stiffness interfacial region is comparable to the width of the shock front. Thus, the continuum-level assumption of sharp (discontinuous) interfaces/shock fronts begins to break down for thin domains and weak shocks. This is consistent with finding the largest underpredictions by the theory for weak shocks, where the shock front is broadest. Together, these factors provide a reasonable explanation for the reduced reflection from thin amorphous domains, and for the discrepancy between theory and simulation for weak shocks. Furthermore, they suggest an explanation for the lower-than-expected energy reflection from amorphous domains (two interfaces) relative to single interfaces: even the largest (50 nm) amorphous pockets studied here are still subject to confinement and finite-size effects. Therefore, amorphous inclusions must be even larger (>50 nm) to maximize energy reflection and shock attenuation.

The significance of these results emerges as a design choice for specific applications. Processing techniques can be used to tune the size and distribution of amorphous domains and therefore shock attenuation. Applications requiring rapid, local attenuation of shock waves may benefit from large amorphous pockets. Other applications, requiring minimal attenuation and rapid propagation of energy over a wide area, may instead benefit from small amorphous pockets. Furthermore, our results suggest a design strategy that exploits the geometry—size and location—of amorphous domains. For example, areas of small amorphous regions would allow rapid energy transfer to neighboring areas of large amorphous regions for energy absorption. This concept of shock wave attenuation by engineering the geometry of impedance-mismatched regions has been studied at the macroscale [80–82], where significant benefits have been achieved, but more study is required to enable such design at the nanoscale. Furthermore, our results may prove useful, by analogy, for shock attenuation and dispersion in laminate composites, which typically contain numerous alternating hard/soft layers [83,84].

Along these lines, we discuss aspects of the present work that could be expanded upon or improved in future studies. (1) From an engineering perspective, it would be useful to find the minimum dimension at which confinement effects in amorphous regions disappear and energy reflection plateaus. Our experience here indicates that larger simulation models (>300 nm in the direction of shock) are necessary to study larger (>50 nm) amorphous pockets. (2) The united-atom force field used here does not accurately capture temperature changes, due to the reduction in degrees of freedom. A natural extension of the present work is to employ an all-atom force field to examine temperature effects, such as hot-spot formation. Additionally, using a reactive all-atom force field would

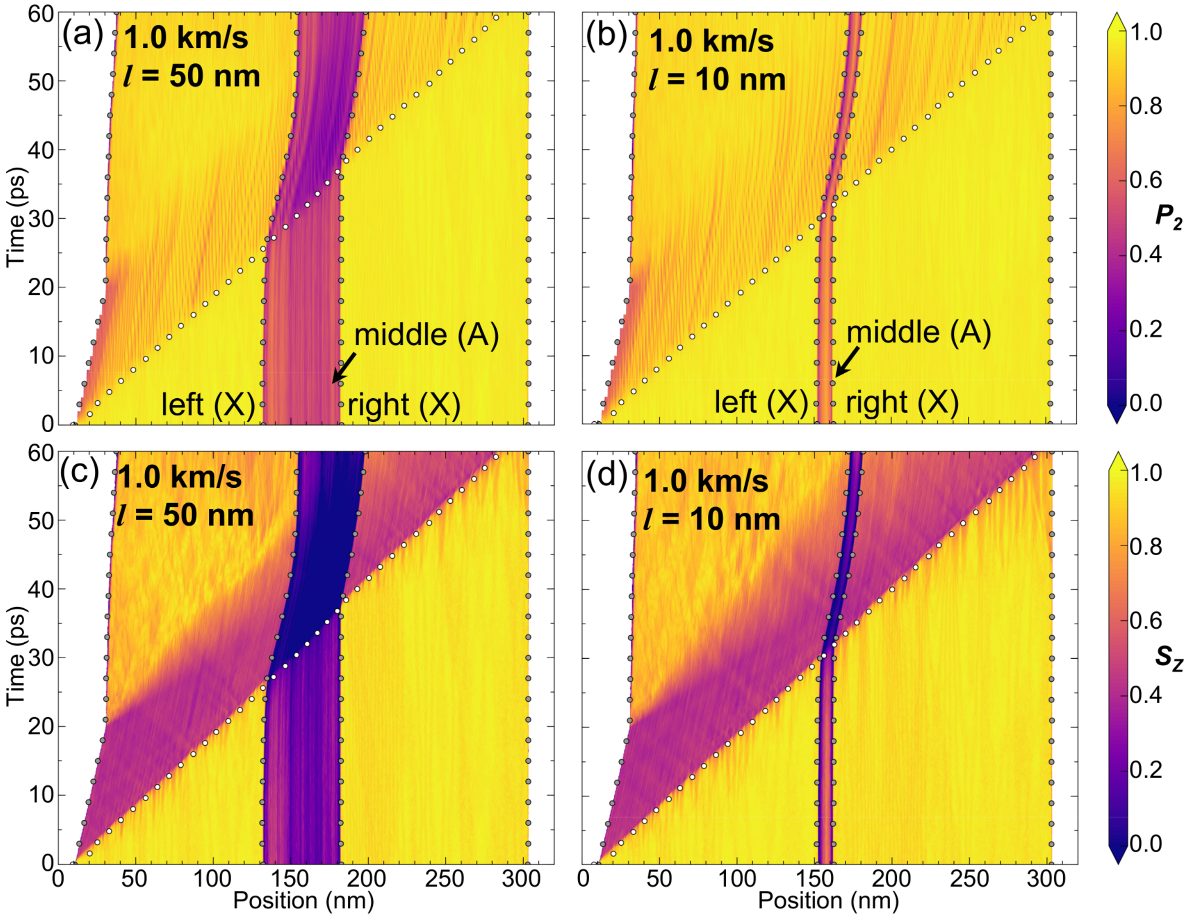

FIG. 11. Ordering and alignment of PE chains. Position-time diagrams of: chain order parameter P_2 in the (a) L50 and (b) L10 systems; and chain alignment with the direction of shock (the $+z$ direction) S_Z in the (c) L50 and (d) L10 systems. The piston velocity is 1.0 km/s, and the piston pulse duration is 20 ps.

enable the study of stronger shocks and other modes of shock loading, such as tension or shear, where chemical reactions are likely [15]. (3) Previous studies show that crystalline chains are tilted with respect to crystalline/amorphous interfaces [32,34,38–40], i.e., along the {201} crystallographic plane rather than {001} as assumed here. Furthermore, even purely crystalline PE will show interesting anisotropic behavior depending on the chain orientation relative to the shock. A detailed study of shock along various crystallographic planes would improve our understanding of the mechanisms of plasticity in crystalline PE [85]. (4) We have not studied the effects of chain topology in the amorphous region (e.g., bridging chains, entanglements). Topology is critical for other deformation modes, such as with bridges in semicrystalline polymers and entanglements in amorphous polymers during tensile deformation [39,40,86–88]. Thus topology will be relevant for tensile waves, which can cause chain scission and fracture. Another interesting possibility is a relation between chain topology and mobility in amorphous regions, because certain topological features may limit mobility, thereby enhancing stiffness and shock propagation. Overall, a systematic study of chain topology would be valuable. (5) More generally, and related to the crystallographic orientation and chain topology, the structure of the interphase region may influence shock propagation. Accurately constructing and characterizing the interphase remains an area of intense study [32–40,49]. For computational efficiency we used an expedient method to construct amorphous regions, but future studies could incorporate more sophisticated algorithms [35]. Furthermore, explicitly examining the effect of the interphase stiffness gradient and the width of the shock front, perhaps with an approach like that in Ref. [63], would enable an explicit test of the various connections we have postulated. (6) The theoretical calculations used here are admittedly simplistic. Developing a more advanced continuum-level framework—ideally, one accounting for plasticity, anisotropy, and the molecular-level effects observed here—would enable accurate prediction of shock attenuation, e.g., in complex geometries. Each of these future directions has the potential to improve the performance of semicrystalline polymers in practical applications.

ACKNOWLEDGMENTS

We thank J. D. Moore and J. K. Brennan for preliminary simulations and fruitful discussions. The authors are grateful to G. A. Gazonas and M. A. Tschopp for a critical reading of the manuscript. R.M.E. and I.C.Y. were supported by an appointment to the Postgraduate Research Participation Program at the U.S. Army Research Laboratory (ARL) administered by the Oak Ridge Institute for Science and

Education through an interagency agreement between the U.S. Department of Energy and ARL. T.O. and M.R. performed this research within the Center for Materials in Extreme Dynamic Environments (CMEDE) under the Hopkins Extreme Materials Institute at Johns Hopkins University. Financial support was provided by the Army Research Laboratory under the MEDE Collaborative Research Alliance, through Grant No. W911NF-12-2-0022 and by the Modeling Complex Systems IGERT, through Grant No. DGE0801471. This work was supported by grants of computer time from the DoD High Performance Computing Modernization Program at the U.S. Air Force Research Laboratory DoD Supercomputing Resource Center (DSRC), the U.S. Army Engineer Research and Development Center DSRC, the U.S. Navy DSRC, and the Maui High Performance Computing Center DSRC. The research reported in this document was performed in connection with contract W911QX-16-D-0014 with ARL. The views and conclusions contained in this document are those of SURVICE Engineering Company, Bennett Aerospace, Inc., and ARL. Citation of manufacturer's or trade names does not constitute an official endorsement or approval of the use thereof. The U.S. Government is authorized to reproduce and distribute reprints for Government purposes notwithstanding any copyright notation hereon.

---

[1] S. Jacobsen and H. G. Fritz, Polym. Eng. Sci. **39**, 1303 (1999).
[2] W. G. Hu and K. Schmidt-Rohr, Polymer **41**, 2979 (2000).
[3] V. M. Litvinov, J. Xu, C. Melian, D. E. Demco, M. Möller, and J. Simmelink, Macromolecules **44**, 9254 (2011).
[4] J. H. Kim, N. A. Heckert, K.-L. Kang, W. G. McDonough, K. D. Rice, and G. A. Holmes, in *Dynamic Behavior of Materials, Volume 1: Proceedings of the 2015 Annual Conference on Experimental and Applied Mechanics*, edited by B. Song *et al.* (Springer International Publishing, Berlin, 2016), p. 69.
[5] S. H. Lee and A. M. Waas, Int. J. Fract. **100**, 275 (1999).
[6] N. Fleck, Adv. Appl. Mech. **33**, 43 (1997).
[7] P. J. Hazell, G. J. Appleby-Thomas, X. Trinquant, and D. J. Chapman, J. Appl. Phys. **110**, 043504 (2011).
[8] W. J. Carter and S. P. Marsh, Los Alamos National Laboratory Report No. LA-13006-MS, 1995.
[9] Y. Mori and K. Nagayama, Rev. High Pressure Sci. Technol. **7**, 841 (1998).
[10] W. Nellis, F. H. Ree, R. Trainor, A. Mitchell, and M. Boslough, J. Chem. Phys. **80**, 2789 (1984).
[11] J. C. F. Millett and N. K. Bourne, J. Phys. D: Appl. Phys. **37**, 2901 (2004).
[12] T. R. Mattsson, J. M. D. Lane, K. R. Cochrane, M. P. Desjarlais, A. P. Thompson, F. Pierce, and G. S. Grest, Phys. Rev. B **81**, 054103 (2010).
[13] P. L. Theofanis, A. Jaramillo-Botero, W. A. Goddard, T. R. Mattsson, and A. P. Thompson, Phys. Rev. B **85**, 094109 (2012).
[14] T. L. Chantawansri, T. W. Sirk, E. F. C. Byrd, J. W. Andzelm, and B. M. Rice, J. Chem. Phys. **137**, 204901 (2012).
[15] T. C. O'Connor, J. Andzelm, and M. O. Robbins, J. Chem. Phys. **142**, 024903 (2015).
[16] J. B. Maillet, M. Mareschal, L. Soulard, R. Ravelo, P. S. Lomdahl, T. C. Germann, and B. L. Holian, Phys. Rev. E **63**, 016121 (2000).
[17] D. Bedrov, J. B. Hooper, G. D. Smith, and T. D. Sewell, J. Chem. Phys. **131**, 034712 (2009).
[18] E. J. Reed, L. E. Fried, and J. D. Joannopoulos, Phys. Rev. Lett. **90**, 235503 (2003).
[19] V. Agrawal, P. Peralta, Y. Li, and J. Oswald, J. Chem. Phys. **145**, 104903 (2016).
[20] F. Xie, Z. Lu, Z. Yang, W. Hu, and Z. Yuan, Polymer **98**, 294 (2016).
[21] T. L. Chantawansri, I.-C. Yeh, T. W. Sirk, J. D. Moore, J. K. Brennan, and J. W. Andzelm, *MACH Conference* (Annapolis, MD, 2014).
[22] S. Root, T. A. Haill, J. M. D. Lane, A. P. Thompson, G. S. Grest, D. G. Schroen, and T. R. Mattsson, J. Appl. Phys. **114**, 103502 (2013).
[23] J. M. D. Lane, G. S. Grest, and T. R. Mattsson, Comput. Mater. Sci. **79**, 873 (2013).
[24] Y. Fu, J. Michopoulos, and J.-H. Song, J. Polym. Sci., Part B: Polym. Phys. **53**, 1292 (2015).
[25] L. He, T. D. Sewell, and D. L. Thompson, J. Appl. Phys. **114**, 163517 (2013).
[26] M. G. Fröhlich, T. D. Sewell, and D. L. Thompson, J. Chem. Phys. **140**, 024902 (2014).
[27] B. Arman, Q. An, S. N. Luo, T. G. Desai, D. L. Tonks, T. Çağın, and W. A. Goddard, J. Appl. Phys. **109**, 013503 (2011).
[28] M. Grujicic, B. Pandurangan, W. C. Bell, B. A. Cheeseman, C.-F. Yen, and C. L. Randow, Mater. Sci. Eng., A **528**, 3799 (2011).
[29] S. Jiang, T. D. Sewell, and D. L. Thompson, J. Phys. Chem. C **120**, 22989 (2016).
[30] L. Barker, C. Lundergan, P. Chen, and M. Gurtin, J. Appl. Mech. **41**, 1025 (1974).
[31] O. E. Petel, F. X. Jetté, S. Goroshin, D. L. Frost, and S. Ouellet, Shock Waves **21**, 215 (2011).
[32] S. Lee and G. C. Rutledge, Macromolecules **44**, 3096 (2011).
[33] S. Balijepalli and G. C. Rutledge, J. Chem. Phys. **109**, 6523 (1998).
[34] S. Gautam, S. Balijepalli, and G. C. Rutledge, Macromolecules **33**, 9136 (2000).
[35] P. J. in't Veld and G. C. Rutledge, Macromolecules **36**, 7358 (2003).
[36] P. J. in't Veld, M. Hütter, and G. C. Rutledge, Macromolecules **39**, 439 (2006).
[37] M. Hütter, P. J. in't Veld, and G. C. Rutledge, Polymer **47**, 5494 (2006).
[38] J. M. Kim, R. Locker, and G. C. Rutledge, Macromolecules **47**, 2515 (2014).
[39] I.-C. Yeh, J. W. Andzelm, and G. C. Rutledge, Macromolecules **48**, 4228 (2015).
[40] I.-C. Yeh, J. L. Lenhart, G. C. Rutledge, and J. W. Andzelm, Macromolecules **50**, 1700 (2017).
[41] W. Paul, D. Y. Yoon, and G. D. Smith, J. Chem. Phys. **103**, 1702 (1995).
[42] J. Chang, J. Han, L. Yang, R. L. Jaffe, and D. Y. Yoon, J. Chem. Phys. **115**, 2831 (2001).

[43] See Supplemental Material at http://link.aps.org/supplemental/10.1103/PhysRevMaterials.1.043606 for a comparison of methods of amorphization, and results for energy reflection measured using energy flux. Inputs for an MD simulation with LAMMPS of PE oligomers using the force field employed in this work are also included. The following references are cited: [14,44,57,66,67,89].

[44] S. Plimpton, J. Comp. Phys. **117**, 1 (1995).

[45] T. Schneider and E. Stoll, Phys. Rev. B **17**, 1302 (1978).

[46] H. J. C. Berendsen, J. P. M. Postma, W. F. van Gunsteren, A. DiNola, and J. R. Haak, J. Chem. Phys. **81**, 3684 (1984).

[47] A. V. Bolesta, L. Zheng, D. L. Thompson, and T. D. Sewell, Phys. Rev. B **76**, 224108 (2007).

[48] M. J. Cawkwell, T. D. Sewell, L. Zheng, and D. L. Thompson, Phys. Rev. B **78**, 014107 (2008).

[49] K. J. Fritzsching, K. Mao, and K. Schmidt-Rohr, Macromolecules **50**, 1521 (2017).

[50] E. O. Lebigot, computer code Uncertainties: a Python package for calculations with uncertainties, v3.0.1, http://pythonhosted.org/uncertainties/.

[51] A. P. Thompson, S. J. Plimpton, and W. Mattson, J. Chem. Phys. **131**, 154107 (2009).

[52] T. S. Yankova, A. Y. Bobrovsky, and A. K. Vorobiev, J. Phys. Chem. B **116**, 6010 (2012).

[53] W. Humphrey, A. Dalke, and K. Schulten, J. Mol. Graphics **14**, 33 (1996).

[54] A. Stukowski, Model. Simul. Mater. Sci. Eng. **18**, 015012 (2010).

[55] L. Davison, *Fundamentals of Shock Wave Propagation in Solids* (Springer, Berlin, 2008).

[56] A. Haselbacher, Shock Waves **22**, 381 (2012).

[57] D. J. Pastine, *Colloque Internationale du C.N.R.S. sur Les Propriétés Physiques des Solides Sous Pression* (Centre National de la Recherche Scientifique, Grenoble, France, 1969).

[58] B. L. Holian, Shock Waves **5**, 149 (1995).

[59] H. Hosseini, S. Moosavi-Nejad, H. Akiyama, and V. Menezes, Appl. Phys. Lett. **104**, 103701 (2014).

[60] A. M. Loske, *Medical and Biomedical Applications of Shock Waves* (Springer International Publishing, Berlin, 2016).

[61] J. W. Forbes, *Shock Wave Compression of Condensed Matter: A Primer* (Springer, Berlin, 2013).

[62] Furthermore, it should be noted that after crossing an interface the particle velocity differs from the piston velocity due to the impedance change. The new particle velocity, and the corresponding shock velocity, can be calculated using the impedance-matching technique [e.g., L. Davison, *Fundamentals of Shock Wave Propagation in Solids* (Springer, Berlin, 2008)]. We performed these calculations, finding that the fraction of reflected energy was reduced but that the qualitative trend of decreasing reflection with increasing shock strength was maintained. Additionally, this correction introduces an asymmetry in energy reflection depending on the phase from which the shock originates. As our intent is to show the qualitative effect of crystalline/amorphous interfaces, in the interest of brevity we use values of Z without correction using the impedance-matching technique.

[63] H. A. Bruck, Int. J. Solids Struct. **37**, 6383 (2000).

[64] O. A. Hurricane and P. L. Miller, Lawrence Livermore National Laboratory Report No. UCRL-ID-132586, 1998.

[65] J. Karnesky, J. Damazo, K. Chow-Yee, A. Rusinek, and J. E. Shepherd, Int. J. Solids Struct. **50**, 97 (2013).

[66] L. F. Henderson, in *Handbook of Shock Waves*, edited by G. Ben-Dor, O. Igra, and T. Elperin (Academic Press, New York, 2001).

[67] R. J. Hardy, J. Chem. Phys. **76**, 622 (1982).

[68] Precompression was accomplished by scaling the system affinely in the z direction over 100 ps and then equilibrating for another 100 ps. Because the system is nonperiodic in z, we enforced the shorter length (and higher density) with harmonic walls above and below the sample in the z direction. We used NVT MD with the same methods as for other equilibrations during this compression process. Then, we shock the precompressed amorphous system with varying piston velocities to generate the Hugoniot

[69] P. Thamburaj, M. H. Santare, and G. A. Gazonas, J. Eng. Mater. Technol. **125**, 412 (2003).

[70] H.-W. Hu and S. Granick, Science **258**, 1339 (1992).

[71] P. A. O'Connell, J. Wang, T. A. Ishola, and G. B. McKenna, Macromolecules **45**, 2453 (2012).

[72] K. A. Page, A. Kusoglu, C. M. Stafford, S. Kim, R. J. Kline, and A. Z. Weber, Nano Lett. **14**, 2299 (2014).

[73] W. Xia, J. Song, D. D. Hsu, and S. Keten, Macromolecules **49**, 3810 (2016).

[74] X. Cheng, K. W. Putz, C. D. Wood, and L. C. Brinson, Macromol. Rapid Commun. **36**, 391 (2015).

[75] R. M. Elder, J. W. Andzelm, and T. W. Sirk, Chem. Phys. Lett. **637**, 103 (2015).

[76] P.-H. Lin and R. Khare, Macromolecules **43**, 6505 (2010).

[77] Z. Fakhraai and J. A. Forrest, Science **319**, 600 (2008).

[78] P. M. Chaikin and T. C. Lubensky, *Principles of Condensed Matter Physics* (Cambridge University Press, Cambridge, 2000).

[79] D. Hui and P. K. Dutta, Composites, Part B **42**, 2181 (2011).

[80] X. Luo, A. Aref, and G. Dargush, J. Comput. Civil Eng. **26**, 387 (2011).

[81] Y.-C. Liu and J. H. Huang, Composites, Part B **43**, 1649 (2012).

[82] R. Rafiee-Dehkharghani, A. J. Aref, and G. F. Dargush, Composites, Part B **75**, 307 (2015).

[83] S. Zhuang, G. Ravichandran, and D. E. Grady, J. Mech. Phys. Solids **51**, 245 (2003).

[84] A. Molinari and G. Ravichandran, J. Mech. Phys. Solids **54**, 2495 (2006).

[85] T. C. O'Connor, R. M. Elder, Y. R. Sliozberg, T. W. Sirk, J. W. Andzelm, and M. O. Robbins, Phys. Rev. Mater. (to be published).

[86] T. Ge, G. S. Grest, and M. O. Robbins, Macromolecules **47**, 6982 (2014).

[87] Y. Men, J. Rieger, and G. Strobl, Phys. Rev. Lett. **91**, 095502 (2003).

[88] D. Hossain, M. A. Tschopp, D. K. Ward, J. L. Bouvard, P. Wang, and M. F. Horstemeyer, Polymer **51**, 6071 (2010).

[89] Y. R. Sliozberg, M. Kröger, and T. L. Chantawansri, J. Chem. Phys. **144**, 154901 (2016).